The dynamo properties of the reversed field pinch velocity field

Robert Chahine, Wouter J.T. Bos, Nicolas Plihon

The dynamo properties of the RFP velocity field

Robert Chahine,[1] Wouter J.T Bos,[1] and Nicolas Plihon[2]
[1)] *Univ Lyon, CNRS, Ecole Centrale de Lyon, INSA Lyon, Univ Claude Bernard Lyon 1, LMFA, UMR5509, 69340 Ecully, France*
[2)] *Univ Lyon, ENS de Lyon, CNRS, Laboratoire de Physique, F-69342 Lyon, France*[a)]

(Dated: 9 February 2022)

The reversed field pinch (RFP) is a toroidal device aiming at the magnetic confinement of a plasma in order to reach conditions of thermonuclear reactions. In RFPs the magnetic and velocity field self-organize to a saturated state determined by their nonlinear interplay and the values of the transport-coefficients. The question addressed in this article is whether this saturated velocity-field is capable of amplifying a seed magnetic field, the so-called dynamo-effect for the astrophysical community. It is shown, using numerical simulations in periodic cylinders, that the RFP velocity field can amplify a passively advected seed-field, but that this is only observed for values of the magnetic Prandtl number above unity. These observations are reported for both laminar and turbulent RFP flows. We further assess the difference in behaviour between a passively advected vector field and the true magnetic field and show that their difference is associated with the detailed alignment properties of the fields.

I. INTRODUCTION

In the context of geophysics and astrophysics, the dynamo instability is the process, now widely accepted, to be at the origin of magnetic fields of astrophysical bodies[1]. The dynamo instability converts kinetic energy into magnetic energy for certain types of flows of electrically conducting fluids[2]. There exist a number of anti-dynamo theorems which restrict the occurrence of the dynamo instability to specific classes of flows[2,3] and the observation of the dynamo instability in experiments is currently restricted to a few realisations in liquid metals[4] or plasma flows[5] which were carefully optimized to obtain critical values for the magnetic Reynolds number of the order of a few dozens. While there has been a great deal of interest for dynamo features in spherical geometries in the context of the geodynamo[6] or the solar dynamo[7], dynamos were also investigated in toroidal geometries. Torus dynamos were in particular proposed as a paradigm for the accretion disk dynamo[8,9]. At the experimental level, several studies considered the screw dynamo in a torus[10]. In this configuration, a liquid metal helical flow is generated from the sudden deceleration of the torus, and the critical magnetic Reynolds was determined to be above 18 after careful optimization of the liquid flow[11,12].

The dynamical growth of the dynamo magnetic energy is usually separated as a two-step evolution. During a first step, also called the kinematic dynamo, a small magnetic field is amplified by a velocity field, which is negligibly influenced by the Lorentz force. During this first step we can therefore individually evolve the velocity field and the magnetic field, since the latter is too weak to influence the former. The second step consists of the saturation phase, where the magnetic field has grown strong enough to back-react on the velocity field by means of the Lorentz-force. In this second phase the simultaneous evolution of both fields should therefore be considered in detail to correctly describe the coupled dynamics of the fields.

In the plasma fusion community, dynamo regimes usually refer to regimes where an electromotive force is induced by flow and magnetic field fluctuations due to turbulence, and has been reported for most of the magnetically-confined fusion plasma configurations, such as Reversed Field Pinches (RFPs), spheromaks or tokamaks. The current profile observed in RFPs was proposed to be sustained by a dynamo regime due to continuous chaotic or turbulent motion[13–15]. Investigations in various regimes were reported over the last two decades [16–20]. More recently, a dynamo electromotive force was proposed to explain stationary non-sawtoothing regimes in tokamaks, often referred to as "flux pumping" [21–23]. However, in essence, in the context of fusion plasma, the nature of the dynamo is fairly different from the astrophysical dynamo, in particular in the kinematic phase, since the initial magnetic field is not a weak small-scale background, but a strong large-scale imposed field.

The astrophysical and fusion plasma communities do therefore not address exactly the same subject when they discuss the dynamo effect. It is this semantic difference which motivated the present study, but we think that the findings might be important beyond this semantic motivation. The precise question we address is whether the velocity field, spontaneously generated through MHD instabilities in RFP geometries can give rise to a dynamo effect in the astrophysical sense. To do so, we carry out MHD simulations in a periodic cylinder in the RFP regime and characterize its capacity to amplify a seed field. For this we will consider an auxiliary magnetic field which is passively advected by the plasma flow.

Our approach is similar to the one adopted in the investigation by Cattaneo and Tobias[24] who investigated a convectively driven saturated dynamo-velocity field. Indeed, this approach allows to explore how the capacity of

[a)]Corresponding author: nicolas.plihon@ens-lyon.fr

a velocity field to amplify a seed-field changes when the induced magnetic field is large enough to saturate the velocity field. In the present investigation we transpose these ideas to the flow generated in an RFP.

The remainder of this article is constructed as follows. The governing equations and normalization are given in the next section, together with a description of the numerical method, set-up and boundary conditions. The results are presented in Secs. III and IV, where we consider the kinematic dynamo in a frozen laminar velocity field, and for a turbulent velocity field, respectively. Sec. V concludes this investigation.

II. RFP SIMULATIONS AND ADVECTION OF PASSIVE VECTOR FIELDS

The goal of this article is to investigate whether the velocity field spontaneously generated through MHD instabilities in RFPs may sustain a dynamo effect. We thus adopted the following methodology:

- A first set of MHD equations (Eqs. (1)-(4) below) are solved for the magnetic field $\boldsymbol{B}$ and the velocity field $\boldsymbol{u}$ in a cylindrical geometry, with initial and boundary conditions corresponding to that of an RFP (applied axial magnetic field and imposed axial electric current). The initial condition for the velocity field is small random noise and, as time evolves, a kink instability develops and generates a flow. The resulting RFP flow back reacts on the magnetic field and finally reaches a statistically stationary state, referred to as the RFP velocity field.
- We then use this statistically stationary RFP velocity field as an externally prescribed flow in an induction equation for an auxiliary passive magnetic field $\boldsymbol{D}$ (Eqs (5)-(6) below). The questions addressed in this article are thus similar to a kinematic dynamo study: (i) does the RFP velocity field lead to exponential growth of passive magnetic energy starting from an initially infinitesimal seed passive magnetic field ?, (ii) what are the growing eigenmodes of the passive induction equation ?

Let us now describe in detail the set of equations, numerical methods, and the boundary and initial conditions.

A. MHD simulations of the RFP magnetic and velocity fields

The simplest geometry in which the RFP can be investigated theoretically and numerically is the periodic cylinder. By solving the MHD equations in such a domain, combined with imposed axial magnetic and electric fields, the resulting dynamics bear a resemblance with actual RFP dynamics. Indeed, for certain values of the imposed fields, MHD instabilities lead to the generation of a velocity field, which in turn back-reacts on the magnetic field by means of the Lorentz force. The periodic cylinder constitutes therefore a paradigm in RFP research, which originates from pioneering works[25–28], but is still actively considered[29,30], since it allows to disentangle the effects of curvature or toroidicity from the already complex dynamics[31].

In the following we will thus consider MHD simulations in a periodic cylinder. The RFP velocity field $\boldsymbol{u}$ is generated by a kink-instability resulting from its interaction with the RFP magnetic field $\boldsymbol{B}$ and current density $\boldsymbol{j}$. These fields are governed by the equations:

$$\frac{\partial \boldsymbol{u}}{\partial t} + (\boldsymbol{u}\cdot\nabla)\boldsymbol{u} = -\nabla P + \boldsymbol{j}\times\boldsymbol{B} + \nu\nabla^2\boldsymbol{u}, \quad (1)$$

$$\frac{\partial \boldsymbol{B}}{\partial t} = \nabla\times(\boldsymbol{u}\times\boldsymbol{B}) + \lambda\nabla^2\boldsymbol{B}, \quad (2)$$

$$\boldsymbol{\nabla}\cdot\boldsymbol{u} = 0, \quad (3)$$

$$\boldsymbol{\nabla}\cdot\boldsymbol{B} = 0 \quad (4)$$

where ν is the kinematic viscosity, λ is the magnetic diffusivity, and P is the pressure. This form of the equations corresponds to a normalization of the velocity by the Alfvén velocity $C_A = B^{(0)}/\sqrt{\mu_0\rho}$, with $B^{(0)}$ the imposed magnetic field, ρ the fluid density and μ_0 the vacuum magnetic permeability. Analogously, an Alfvén timescale is introduced as $t_A = L/C_A$. The magnetic field consists of a freely evolving component plus an imposed mean field, described below. The characteristic lengthscale L is equal to the diameter of the cylinder $2R$. The control parameter of these equations is the Lundquist number $S = C_A L/\lambda$, which controls the amplitude of the velocity field, and thus of the kinetic Reynolds number $Re = UL/\nu$, where the characteristic velocity U is chosen equal to the RMS velocity. For simplicity, and following a long-standing practice in dynamo theory[3,24] we restrict ourselves to the case where $\nu = \lambda$, or in other words, the magnetic Prandtl number is taken to be equal to unity. This assumption allows to avoid scale separation between the magnetic and velocity fields, thus limiting the already large computational cost and allowing to explore several regimes. Note that since the magnetic Prandtl number is unity, the magnetic Reynolds number Rm associated with the B-field is equal to the kinetic Reynolds number Re.

Eqs. (1)-(4) are solved in a periodic cylinder of length 8π, and diameter $2R = 2$. The MHD-domain is solved in a larger rectangular box of $\pi\times\pi\times 8\pi$, where the solid boundaries are imposed using a penalization method. The evolution equations are computed using a pseudo-spectral solver with a 3rd order Adams-Bashforth time-integration scheme. Details on the numerical methods and its convergence properties can be found in a previous publication[32]. In the present simulations the resolution is $64\times 64\times 512$ grid-points in the x, y, z-directions, respectively. The pressure is computed from the resolution of the Poisson equation in the spectral domain[33] The initial magnetic field is a combination of an axial field

$B_z^{(0)} = 0.2$ and a poloidal field $B_p^{(0)}(R) = 1.4$ at the wall, associated with a uniform imposed axial current density $j_z^{(0)}(r) = 2.8$. The axial component of the magnetic field at the boundaries is left unconstrained. The velocity-field is satisfying no-slip boundaries at the wall.

For all simulations the initial conditions are small amplitude random noise for the velocity field and zero value for the non-imposed contribution of the magnetic field. After a short transient, the non-linear interactions between the velocity field $\boldsymbol{u}$ and the magnetic field $\boldsymbol{B}$ lead to the generation of flows $\boldsymbol{u}_{\mathrm{RFP}}$ in the RFP, whose features are discussed in Secs. III A and IV for diffferent values of the Lundquist number S, which is varied through the value of the diffusivities $\lambda = \nu$. The resulting statistically stationary velocity field is then used as a prescribed velocity field in the auxiliary passive induction equation (see next subsection) in kinematic dynamo simulations.

B. Auxiliary passive magnetic field dynamics

In addition to the set of Eqs.(1)-(4), we solve the evolution of an auxiliary passive field $\boldsymbol{D}$, satisfying the equations,

$$\frac{\partial \boldsymbol{D}}{\partial t} = \nabla \times (\boldsymbol{u} \times \boldsymbol{D}) + \lambda' \nabla^2 \boldsymbol{D}, \qquad (5)$$

$$\boldsymbol{\nabla} \cdot \boldsymbol{D} = 0. \qquad (6)$$

where λ' is the magnetic diffusivity of the passive field $\boldsymbol{D}$ (quantities related to the passive magnetic field $\boldsymbol{D}$ are primed in order to avoid any confusion with quantities related to $\boldsymbol{B}$). Note that the equations governing the dynamics of $\boldsymbol{D}$ are identical to the induction equations (Eqs. (2),(4)). The three differences between $\boldsymbol{D}$ and $\boldsymbol{B}$ are that firstly, $\boldsymbol{D}$ does not back-react on the velocity field by the Lorentz force, secondly that $\boldsymbol{D}$ does not contain an imposed contribution. The third difference is that the magnetic diffusivities λ, related to $\boldsymbol{B}$, and λ', related to $\boldsymbol{D}$, are not equal. This is also a difference with the investigation by Cattaneo and Tobias[24], which focused on flows sustaining a dynamo field and for which $\lambda = \lambda'$.

The question that we will answer is whether the velocity field resulting from the interplay of $\boldsymbol{u}$ and $\boldsymbol{B}$ is able to amplify a small seed-field $\boldsymbol{D}$. The control parameter for dynamo action is the magnetic Reynolds number, which compares the induction term to the dissipative term, here for the passive magnetic field D, and defined as $Rm' = UL/\lambda'$. For a given value of the Lundquist number, the amplitude and structure of the RFP velocity field u_{RFP} is prescribed by the values of the imposed axial field $B_z^{(0)}$ and axial current $j_z^{(0)}$, thus the ability of u_{RFP} to sustain a dynamo is assessed by changing Rm' by a change of λ'. The initial passive magnetic field $\boldsymbol{D}$ is a random noise similar to the velocity field, but with initial energy $\langle D^2 \rangle = \int_V D^2 dV \approx 10^{-10}$, where V is the total volume. At the boundary, the poloidal component of $\boldsymbol{D}$ is set to zero.

The set of Eqs. (5)-(6) are solved similarly to Eqs. (1)-(4), in a rectangular box of $\pi \times \pi \times 8\pi$ using the same pseudo-spectral numerical method, and where the solid boundaries are imposed using a penalization method.

Depending on the value of the Lundquist number S, two types of statistically stationary RFP flows are observed after a transient. At low values of S, the flows are are steady and laminar, as reported in Sec. III. In this regime, the laminar steady-state flow $\boldsymbol{u}_{\mathrm{RFP}}$ is prescribed and fixed in time for the auxiliary passive induction equation. Thus, once the laminar flow has been computed, we stopped the computation of the set of MHD equations (1)-(4), and only evolve the auxilary induction equation (5)-(6). At higher values of the Lundquist number S, the RFP flows $\boldsymbol{u}_{\mathrm{RFP}}$ are dynamical and the velocity field exhibits strong fluctuations, as reported in Sec. IV. In this regime, the flow $\boldsymbol{u}_{\mathrm{RFP}}$ prescribed for the auxiliary passive induction equation evolves with time and the set of MHD equations (1)-(4) and passive induction equations (5)-(6) are solved simultaneously. We recall here, that the velocity field $\boldsymbol{u}$ and magnetic field $\boldsymbol{B}$ are fully coupled and that the velocity and magnetic modes reported here are non-linearly saturated. On the other hand, the passive field $\boldsymbol{D}$ does not back react on the velocity field: the modes presented here for the passive field are thus linearly stable or unstable modes, similarly to usual kinematic dynamo computations.

III. LAMINAR DYNAMO SIMULATION FOR THE PASSIVE FIELD.

In this section we will consider cases at low values of the Lundquist number S, for which a steady laminar RFP flow is generated. The features of the velocity field $\boldsymbol{u}$ and magnetic field $\boldsymbol{B}$ are first described, before discussing the onset of dynamo action and the features of the unstable growing mode for the passive dynamo field $\boldsymbol{D}$.

A. A steady Quasi-Single-Helicity state

At first, the steady state laminar flow is computed from the MHD equations (1)-(4), which are solved over a time interval equal to $1500\,\tau_A$. A steady state was reached typically after $200\,\tau_A$. At $t = 1500\,\tau_A$, the RFP magnetic field $\boldsymbol{B}_{\mathrm{RFP}}$ and the flow $\boldsymbol{u}_{\mathrm{RFP}}$ are extracted from the simulations.

The structures of the magnetic field $\boldsymbol{B}_{\mathrm{RFP}}$ and velocity field $\boldsymbol{u}_{\mathrm{RFP}}$ are displayed in Fig. 1(a) and (b) for $S = 150$, where isocontours of the magnetic energy (respectively kinetic energy) are color-coded by the sign of the axial component of the field (which would correspond to the toroidal component in a torus). The magnetic field $\boldsymbol{B}$ has a strong constant axial component (the applied magnetic field), which has been subtracted from the total field in Fig. 1 for the sake of clarity. Both the velocity and the

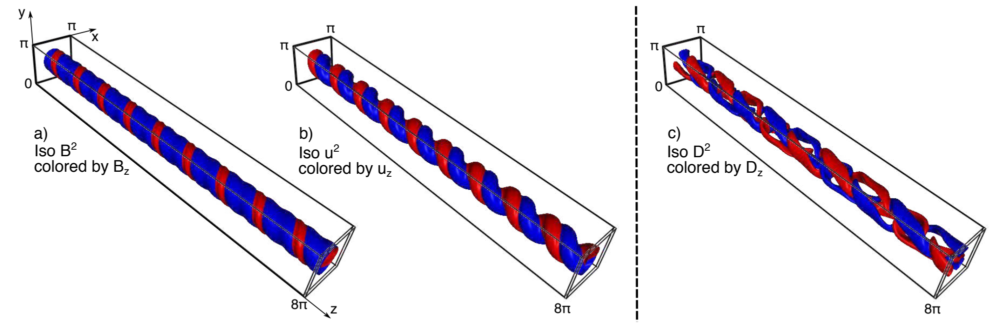

FIG. 1. Visualizations of the kinematic dynamo system. The subfigures (a), (b), (c) show iso-surfaces of B^2, u^2 and D^2, respectively. These isosurfaces are colored by the sign of the axial component. For instance in (a) $B_z > 0$ is colored in red, $B_z < 0$ in blue.

magnetic field display a strong $n = 9$ component, where the mode-number n denotes the axial frequency.

In particular, the flow has a complex structure: it consists of two strongly interlaced helical flows of opposite polarities, as shown by the two red and blue screwed tubes, with a strong shear at the interface between the red and the blue tubes. The steady-state MHD fields generated at $S = 150$ correspond to an intensity of the velocity field leading to a value of the Reynolds number $Re = 6.37$. Such helical flow fields are observed in all simulations, but at low values of S these fields are stationary and laminar, whereas at large values they become time-dependent.

Equations (1)-(4) conserve total energy, magnetic helicity and cross helicity in the limit of vanishing dissipation. The process by which the RFP velocity field $\boldsymbol{u}_{\mathrm{RFP}}$ is created is a conversion of magnetic energy to kinetic energy through a kink instability.[17] As expected for a RFP equilibrium, the field reversal parameter $F = \overline{B_z}/\langle B_z \rangle$ decreases as a function of the pinch ratio, where $\overline{B_z}$ denotes the wall averaged and $\langle B_z \rangle$ the volume-average axial magnetic field. In the present investigation, in both the laminar and turbulent statistically steady states, the equilibrium profile is characterized by a reduced axial magnetic field at the walls $\overline{B_z}$ as compared to the imposed field. This is characteristic of RFPs. However, no reversal is observed (F remains positive) and details on this can be found in Ref. [31].

The flow intensity is measured through the kinetic Reynolds number, shown as a function of the Lundquist number in Fig. 2. The kinetic Reynolds number increases with the Lundquist number, with an empirical scaling $Re \propto S^{0.74}$. Since in these simulations the integral length scale and imposed magnetic field are fixed, this scaling is associated with a dependence of the RMS velocity on the magnetic diffusivity, $U \sim \lambda^{0.26}$. For the lowest values of S and Re this corresponds to steady laminar flow and for the largest values to fluctuating movement with several dominating modes.

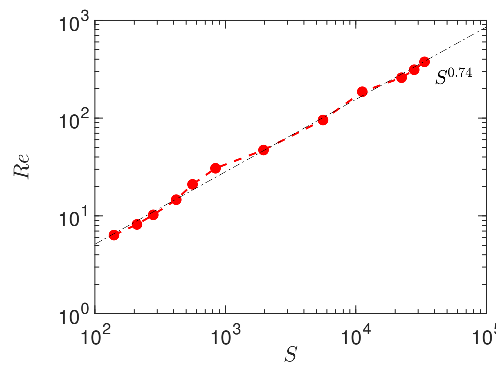

FIG. 2. Lundquist dependence of the Reynolds number in the kinematic dynamo investigation. The Reynolds number is based on the root-mean-square velocity in the domain.

B. The laminar kinematic dynamo.

In this subsection, we investigate the capability of the laminar RFP velocity field $\boldsymbol{u}_{\mathrm{RFP}}$ described in the previous subsection, to induce dynamo action.

The steady state flow $\boldsymbol{u}_{\mathrm{RFP}}$ extracted from the simulations of Eqs. (1)-(4) at $t = 1500\tau_A$, is used as a prescribed field for the passive induction equation (5) starting at time $t = 1500\tau_A$. Th initial condition for the passive field $\boldsymbol{D}$ at $t = 1500\tau_A$ is small Gaussian white noise with initial energy $\langle D^2 \rangle \approx 10^{-10}$. The control parameter governing Eq. (5) is the passive magnetic Reynolds number Rm', which depends upon the passive magnetic diffusivity λ', or equivalently the passive mag-

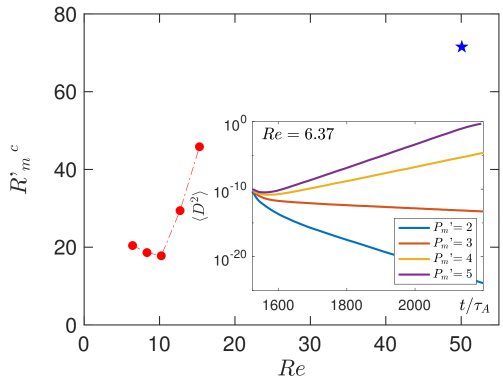

FIG. 3. Evolution of the critical magnetic Reynolds number $R_m'^c$ as a function of the (kinematic) Reynolds number Re. The red, circular data points correspond the kinematic dynamo simulations with a fixed velocity field. The blue, star-shaped data-point corresponds to the result for a fully dynamic simulation, discussed in Sec. IV. The inset shows the time evolution of the passive magnetic energy for different values of P_m' of a given flow with $Re = 6.37$.

netic Prandtl number Pm'. Dynamos are usually observed above a critical magnetic Reynolds number; for a given flow $\boldsymbol{u}_{\mathrm{RFP}}$, we thus expect to excite a passive dynamo field $\boldsymbol{D}$ when increasing Pm'. As an illustration, for $S = 150$, i.e. $Re = 6.37$, the time evolution of the total passive magnetic energy $\langle D^2\rangle$ is displayed in the inset of Fig. 3 for four values of the passive magnetic Prandtl number Pm'. The passive magnetic energy decreases with time for $Pm' \leq 3$ and increases for $Pm' \geq 4$. For $Pm' \geq 4$, after a small transient (around 150 τ_A), i.e. for $t > 1650\tau_A$, the energy of the passive magnetic field increases exponentially with time. For each value of the passive magnetic Prandtl Pm', the growth rate of the passive magnetic energy is computed from the exponential fit of the time evolution of $\langle D^2\rangle$. The critical passive magnetic Prandtl number Pm'^c number is then defined from the linear interpolation of the growth rates between the last negative value and the first positive value, e.g. $Pm'^c = 3.2$ for $Re = 6.37$. This leads to a critical passive magnetic Reynolds number $Rm'^c = Re\ Pm'^c = 20.4$.

A first important observation is that the RFP flow has favorable properties for dynamo generation on a passive magnetic field, which can be qualitatively understood since RFP flows are characterized by high helicity and high shear, two properties which are not necessary but enhance dynamo action[2,3].

Similar simulations have been run for several values of S from 150 to 550 in the laminar regime, and the evolution of the critical passive magnetic Reynolds number as a function of Re is shown in Fig. 3 (only the red points correspond to laminar regimes).

Let us now describe the spatial features of the passive dynamo mode. Figure 1(c) shows the isocontours of the passive magnetic energy D^2, color-coded by the sign of the axial component of the passive field D_z (which would correspond to the toroidal component in a torus). The spatial structure of the passive magnetic field is more complex than the spatial structure of the velocity field. This is further investigated in Fig. 4, left column, where the axial spectra of the magnetic, kinetic and passive magnetic energy are displayed, from top to bottom, for $Re = 6.37$. The discrete modes observed in the spectra for the magnetic and kinetic energies are identical: the dominant RFP mode is the $n = 9$ mode, and harmonics of this mode are clearly observed. The strong harmonics observed in the spectrum of B^2 are a signature of the complex spatial structure observed in Fig.1a) where the blue stripes are larger than the red stripes. We stress here that most of the magnetic energy is contained in the applied $n = 0$ mode (which is not displayed in Fig. 4), less than 11% of the magnetic energy is present at positive mode numbers (precisely 11%, 6.5% and 4.2% for $Re = 6.37, 10.2$ and 15.3 respectively). The dominant mode for the passive magnetic energy $\langle D^2\rangle$ is the $n = 2$ mode, as clearly observed in Fig. 1(c). The induction term $\nabla \times (\boldsymbol{u} \times \boldsymbol{D})$ in the passive induction equation (5) leads to mode mixing between $\boldsymbol{u}$ and $\boldsymbol{D}$, which, for the case at $Re = 6.37$, leads to a complex spectrum for $\langle D^2\rangle$, with strong contributions of modes 7, 11, 16, 20, etc.

The central column of Fig. 4 displays the spectra for the case $S = 276$, e.g. $Re = 10.2$, while the right column corresponds to the case $S = 417$, e.g. $Re = 15.3$. The dominant RFP mode is at $n = 8$, which couples with the dominant $n = 0$ or $n = 10$ modes for $\langle D^2\rangle$, also leading to a complex spectrum for $\langle D^2\rangle$.

We have observed in our simulations that the influence of Pm' on the spectra of D is very weak: the same modes are excited for simulations with values $Pm' = 2, 4, 7$ and only small variations are observed in the relative amplitudes of the modes (not shown).

The strong coupling between the velocity field $\boldsymbol{u}$ and the passive magnetic field $\boldsymbol{D}$ is emphasized in Fig. 5, in which isocontours of the kinetic energy and of the passive magnetic energy are displayed simultaneously for $S = 150$, e.g. $Re = 6.37$. A first observation is that the structure of the passive magnetic field, which is dominated by a $n = 2$ mode is strongly affected by the $n = 9$ dominant velocity mode. This is observed in the zoom of Fig. 5, where the separation between black and white ribbons for the passive magnetic energy (opposite values of D_z) is a zone of strong shear for the velocity field (transition between the red and blue ribbons of the kinetic energy isosurfaces). A second observation is that the kinetic energy is mostly concentrated in the central part of the cylindrical domain, while most of the passive magnetic energy is concentrated in outer radial regions. Another observation is that the structures of the passive magnetic field connect in high velocity shear regions, and the axial component of passive magnetic field reverses sign at the same location as the reversals of the axial

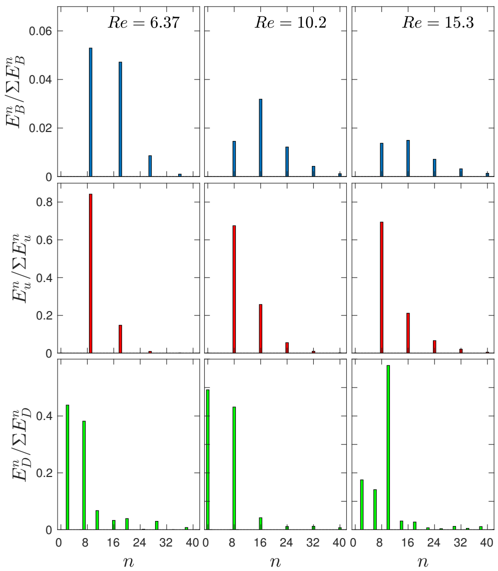

FIG. 4. Normalized axial spectra of B^2 (top), u^2 (center) and D^2 (bottom) for different values of Re and for $P'_m = 4$.

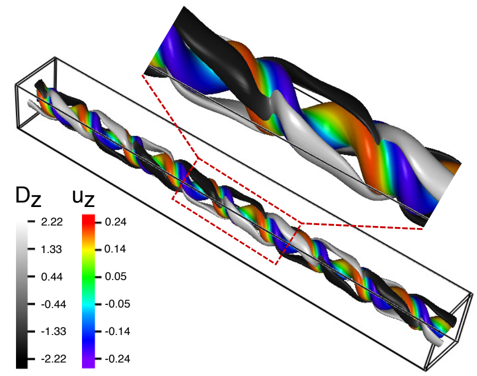

FIG. 5. Visualization of the normalized kinetic energy isosurface, $u^2/\langle u^2\rangle = 6.6$ and the normalized passive magnetic energy isosurface $D^2/\langle D^2\rangle = 9$, colored by the axial velocity field u_z and axial passive magnetic field D_z, respectively, for $Re = 6.37$ and $P'_m = 4$.

component of the velocity field.

To summarize, the laminar RFP flow is a kinematic dynamo velocity field for high enough Pm'. The next question is how the passive and magnetic fields act when the flow is not steady, and how the back-reaction of the magnetic field on the velocity field changes the dynamics.

IV. TURBULENT DYNAMO SIMULATIONS

In this section, we address a regime at large Lundquist number, for which the RFP velocity field $\boldsymbol{u}_{\mathrm{RFP}}$ is no longer steady and laminar. Thus, similarly to the case of convectively driven turbulence investigated by Cattaneo and Tobias [24], simulations are carried out with all three fields $\boldsymbol{u}$, $\boldsymbol{B}$ and $\boldsymbol{D}$ evolving in time. We will first focus on the flow characterization, then we will assess the dynamo threshold and we will finish by evaluating the alignment properties of the system.

A. Flow characterization

Simulations at $S = 2000$, resulting in an RFP flow with $Re = 50$, are carried out, and a snapshot of the kinetic energy is shown in Fig. 6(top). The velocity field clearly shows a trace of a periodic structure, but small scales are also observed. This assessment of the flow-behavior from the flow-visualizations is however of qualitative nature.

A more quantitative characterization of the turbulent nature of the different fields is given by the energy spectra. The axial-mode spectra are shown in Fig. 7. These spectra illustrate that the dynamics of the fields $\boldsymbol{u}$ and $\boldsymbol{B}$ are not restricted to a small number of excited modes. Indeed, the broad-band character of these spectra suggests that the flow is in a turbulent state. Nevertheless, the power-spectra of the velocity and the magnetic field show some well-defined peaks. These peaks are associated with the close to periodic-structure observed in the visualization. Altogether, these broad-band spectra over two decades in wavenumber show that the dynamics in this section are turbulent in the presence of close-to-periodic velocity and magnetic field structures.

In the next subsection we will determine the dynamo-threshold for the present RFP flow.

B. Dynamo growth rate and threshold

The evolution of the passive vector $\boldsymbol{D}$ was solved simultaneously to the dynamical evolution of the $\boldsymbol{u}$ and $\boldsymbol{D}$ fields for $P'_m = 1.43$ and $P'_m = 2$ The time evolution of the mean passive magnetic energy $\langle D^2\rangle$ for these two runs is plotted in Fig. 8. It is observed that for $P'_m = 2$ the RFP field in the dynamic regime is capable of amplifying a seed magnetic field, and the RFP velocity field can therefore be called, as for the laminar case, a dynamo velocity field. In the case of $P'_m = 1.43$, the passive magnetic energy fluctuates around a constant value over a long-time interval. The threshold for dynamo action at $Re = 50$ is therefore close to $P'_m = 1.43$, corresponding to a critical magnetic Reynolds number $R'_{mc} = 71.5$. The new result is added to the data previ-

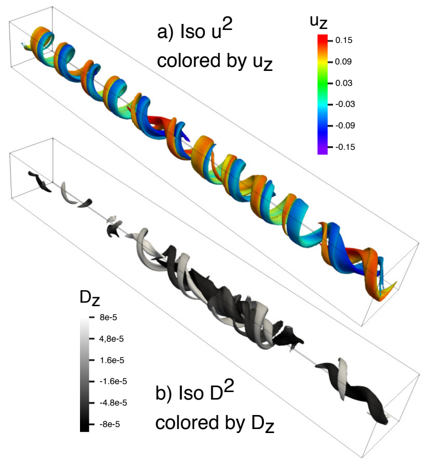

FIG. 6. Visualizations of an instantaneous snapshot of the (a) iso-surfaces of the kinetic energy u^2 and (b) passively advected magnetic energy D^2, colored by the axial component, in the turbulent RFP simulation. Whereas the velocity field seems to be dominated by a small number of energetic modes, the advected field shows a more turbulent behavior.

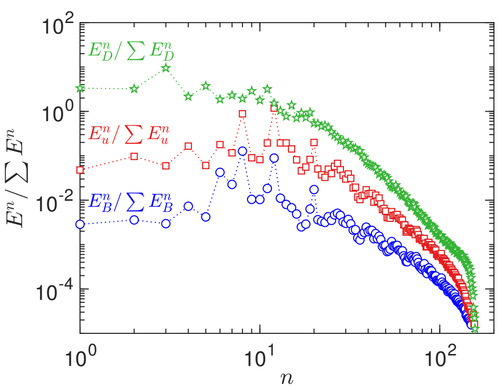

FIG. 7. Normalized spectra of u^2, B^2 and D^2 for $Re = 50$ and $P_m' = 2$. The velocity and passive-vector spectra are shifted upwards for clarity by one and two decades, respectively.

ously obtained in the laminar regime (Figure 3). The critical magnetic Reynolds number in this dynamical case is therefore somewhat higher but of comparable magnitude to the critical value of the laminar kinematic dynamo, observed around $Re = 15$, where $R_{mc}' \approx 50$. We stress here that the resolutions required to well-resolve the dynamics of the passive field $\boldsymbol{D}$ are higher than that required to resolve the $\boldsymbol{u}$ and $\boldsymbol{B}$ fields, resulting in high computational-resource-requirement for turbulent dynamo simulations.

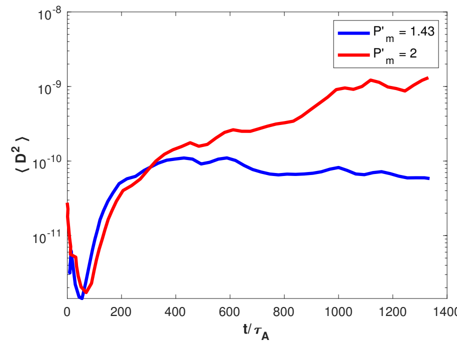

FIG. 8. Time evolution of the variance of the passive field in the dynamic runs for $Re = 50$ and $P_m' = 1.43; 2$.

As a consequence, higher Re regimes are not explored in this manuscript.

A snapshot of the passive magnetic energy at $P_m' = 2$ is shown in Fig. 6 at the same time as the kinetic energy shown in the top panel. As for laminar dynamos, the structure of the passive vector-field $\boldsymbol{D}$ is much more complex than that of the velocity field $\boldsymbol{u}$ and shows a less periodic behavior. This is highlighted by the energy spectrum shown in Fig. 7 which does not display energetic peaks.

The fact that we observe the growth of the amplitude of D^2 in Fig. 8 is in agreement with the observations of[24], who showed that the saturation of the magnetic field $\boldsymbol{B}$ does not modify the velocity field in such a way that dynamo-action is prohibited. Rather it modifies the simultaneous dynamics of $\boldsymbol{B}$ and $\boldsymbol{u}$, such as the alignment properties described later in this section.

We stress here that even though the velocity field is able to amplify a seed-field for certain parameters, this is not the case for $Pm' = 1$. This shows that the diffusive effects acting upon the passive field need to be smaller in our simulations than those acting upon the RFP magnetic field. This seems to indicate that in our simulations the B-field in the statistically steady state is unaffected by the dynamo effect, since its magnetic Reynolds number is below the threshold for dynamo action. This is a major difference compared to the results of[24], where dynamo amplification of a passive field by the saturated velocity field was observed for $Pm' = 1$.

C. Alignment of the different fields

As mentioned above, in ref.[24] the same system of equations was investigated as in the present study, but in a different geometry, using a different forcing. It was observed that the variance of the $\boldsymbol{D}$-field continues to increase after the saturation of the $\boldsymbol{B}$-field. One of the key insights obtained thereby is that the saturation is not only due to the modification of the flow-field by the Lorentz-force. Indeed, if this was the case, the strength of $\boldsymbol{D}$ would saturate simultaneously with that of $\boldsymbol{B}$. Rather is it due to some intricate interplay between the velocity field and the magnetic field. It is therefore not visible from the velocity field alone that the magnetic field saturates, and at which level. One should thus consider the simultaneous dynamics of $\boldsymbol{u}$ and $\boldsymbol{B}$.

One way to consider the simultaneous dynamics of the velocity and the magnetic field is to introduce the Elsasser variables, defined as, $\boldsymbol{z}^{\pm} = \boldsymbol{u} \pm \boldsymbol{B}$, and the passive Elsasser variables, defined as, $\boldsymbol{\xi}^{\pm} = \boldsymbol{u} \pm \boldsymbol{D}$

The dynamical equations for the Elsasser variables are obtained from the sum and the difference of Eqs (1) and (2) yielding

$$\partial_t \boldsymbol{z}^{\pm} + \boldsymbol{z}^{\mp} \cdot \boldsymbol{\nabla} \boldsymbol{z}^{\pm} = \nu \nabla^2 \boldsymbol{z}^{\pm} - \boldsymbol{\nabla} P^*, \tag{7}$$

with $P^* = P + B^2/2$. The dynamical equations for the passive Elsasser variables are obtained from the sum and the difference of Eq (1) and (5), and, using the simplifying assumption $P_m = P'_m = 1$ write

$$\partial_t \boldsymbol{\xi}^{\pm} + \boldsymbol{\xi}^{\mp} \boldsymbol{\nabla} \boldsymbol{\xi}^{\pm} = \nu \nabla^2 \boldsymbol{\xi}^{\pm} - \boldsymbol{\nabla} P^*$$
$$-\frac{1}{4}\left[(\boldsymbol{\xi}^+ - \boldsymbol{\xi}^-) \cdot \nabla(\boldsymbol{\xi}^+ - \boldsymbol{\xi}^-) - (\boldsymbol{z}^+ - \boldsymbol{z}^-) \cdot \boldsymbol{\nabla}(\boldsymbol{z}^+ - \boldsymbol{z}^-)\right], \tag{8}$$

It is insightful to look at the structure of Eqs. (7) and (8) which explicitly expresses the coupling of the different fields. The equations for the Elsasser variables (Eq. (7)) is more symmetric than the equations for the passive Elsasser variables (Eq. (7)), due to the presence of the Lorentz force (and the absence of its passive counterpart).

What this difference exactly implies for the dynamics is not straightforward to infer from the equations. We can however mention the specific case where strong correlations exist between the magnetic field and the velocity field[34,35], such as observed in the solar-wind. In the extreme case of $\boldsymbol{u} = \pm\boldsymbol{B}$, the nonlinear term vanishes for the case of the full system, but does not for the passive advected system. This shows a concrete example of different behavior of the two systems: if the fields are aligned and of equal magnitude, the nonlinearity of the full system is decreased, but not for the passive case.

If the fields align, but are not of equal magnitude, the nonlinearity is weakened, but does not vanish. The tendency for rapid alignment was reported in several studies of incompressible MHD[36–38]. We will here investigate whether the alignment shows a qualitatively different behavior. For this we show in Fig. 9 the probability functions of the cosine of the angle between the different fields at $t = 1200\tau_A$. At instant $t = 0$, the PDF is almost constant (not shown), hence no $(\boldsymbol{u}, \boldsymbol{D})$ alignment is observed. At instant $t = 1200\tau_A$, the PDF reaches two peaks at ± 1 for all three quantities, reflecting preferential alignment and anti-alignment between all three quantities. This local alignment is strongest between the velocity field and the passive field $\boldsymbol{D}$.

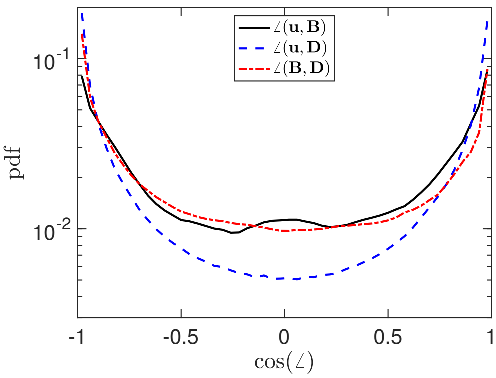

FIG. 9. Probability density functions of the alignment between the three fields during the statistically steady state of the dynamic RFP simulations.

This illustrates that all three vectors locally align with each-other. However, the quantitative difference is not enormous, and the fact that the saturated velocity field is able to amplify the passive seed field is likely to depend on subtle correlations between the magnetic field and the velocity field. We recall that, for the numerical simulations reported here, $P'_m = 1.43 > P_m = 1$ and that the simplifying assumptions leading to the formulation of Eqs. (8) are not strictly fulfilled and that the study of these correlations would require reaching a dynamo regime at $P'_m = 1$.

V. CONCLUSION

The question which motivated the present study was whether the RFP velocity field can amplify a seed-field and can thereby called a dynamo field. The answer to the question is not straightforward. If we do not put any constraints on the diffusivity of the passively advected field, the answer is yes, since both in the laminar, steady case and in the dynamic case we have succeeded to determine a finite value of the critical Reynolds number, as shown in Fig. 3.

In all our simulations we needed however to raise the magnetic Prandtl number of the passive field Pm' above the unity value of the corresponding value for the RFP magnetic field. This shows that fluctuations of the B-field are not subject to the dynamo-effect in the present set-up.

We also traced down a difference in the description of the B and the D field, by considering the Elsasser variables. In particular we showed that alignment of the velocity field and the B-field reduces more strongly the nonlinear interactions than alignment of the D-field with the velocity does.

Exploring in more detail the saturation-mechanism of the turbulent dynamo in terms of detailed alignment properties and Elsasser-dynamics seems a promising direction for further research.

ACKNOWLEDGMENTS

Simulations were carried out using the facilities of the PMCS2I (École Centrale de Lyon), IDRIS (Project No. 22206) and P2CHPD. We further acknowledge support by the French Federation for Magnetic Fusion Studies (FR-FCM) and of the Eurofusion consortium from the Euratom research and training programme 2014–2018 and 2019–2020 under grant agreement No633053. The views and opinions expressed herein do not necessarily reflect those of the European Commission.

[1] J. Larmor, "How could a rotating body such as the sun become a magnet," Rep. Brit. Adv. Sci. , 159–160 (1919).
[2] H. Moffatt, *Magnetic field generation in electrically conducting fluids* (Cambridge University Press, 1978).
[3] F. Rincon, "Dynamo theories," Journal of Plasma Physics **85**, 205850401 (2019).
[4] G. Verhille, N. Plihon, M. Bourgoin, P. Odier, and J.-F. Pinton, "Laboratory dynamo experiments," Space Science Reviews **152**, 543–564 (2010).
[5] P. Tzeferacos, A. Rigby, A. F. A. Bott, A. R. Bell, R. Bingham, A. Casner, F. Cattaneo, E. M. Churazov, J. Emig, F. Fiuza, C. B. Forest, J. Foster, C. Graziani, J. Katz, M. Koenig, C. K. Li, J. Meinecke, R. Petrasso, H. S. Park, B. A. Remington, J. S. Ross, D. Ryu, D. Ryutov, T. G. White, B. Reville, F. Miniati, A. A. Schekochihin, D. Q. Lamb, D. H. Froula, and G. Gregori, "Laboratory evidence of dynamo amplification of magnetic fields in a turbulent plasma," Nature Communications **9**, 591 (2018).
[6] P. H. Roberts and E. M. King, "On the genesis of the earth's magnetism," Reports on Progress in Physics **76**, 096801 (2013).
[7] P. Charbonneau, "Solar dynamo theory," Annual Review of Astronomy and Astrophysics **52**, 251–290 (2014).
[8] W. Deinzer, H. Grosser, and D. Schmitt, "Torus dynamos for galaxies and accretion disks. I. The axisymmetric alpha omega-dynamo embedded into vacuum." Astron. Astrophys. **273**, 405–414 (1993).
[9] E. A. Mikhailov and A. D. Khokhryakova, "Torus dynamo in the outer rings of galaxies," Geophysical & Astrophysical Fluid Dynamics **113**, 199–207 (2019).
[10] A. Chupin, P. Frick, and R. Stepanov, "The screw dynamo in a thick torus," Astronomische Nachrichten **332**, 11–16 (2011), https://onlinelibrary.wiley.com/doi/pdf/10.1002/asna.201011467.
[11] W. Dobler, P. Frick, and R. Stepanov, "Screw dynamo in a time-dependent pipe flow," Phys. Rev. E **67**, 056309 (2003).
[12] D. D. Sokoloff, R. A. Stepanov, and P. G. Frick, "Dynamos: from an astrophysical model to laboratory experiments," Physics-Uspekhi **57**, 292–311 (2014).
[13] C. Gimblett and M. Watkins, "Mhd turbulence theory and its implications for the reversed field pinch," in *Proc. 7th European Conf. on Controlled Fusion and Plasma Phys*, Vol. 1 (1975) p. 103.
[14] H. Strauss, "The dynamo effect in fusion plasmas," The Physics of fluids **28**, 2786–2792 (1985).
[15] A. Yoshizawa and F. Hamba, "A turbulent dynamo model for the reversed field pinches of plasma," The Physics of fluids **31**, 2276–2284 (1988).
[16] D. Bonfiglio, S. Cappello, and D. Escande, "Dominant electrostatic nature of the reversed field pinch dynamo," Physical review letters **94**, 145001 (2005).
[17] D. Escande, "What is a reversed field pinch?" (2013), working paper or preprint.
[18] S. Cappello and D. F. Escande, "Bifurcation in viscoresistive MHD: The Hartmann number and the Reversed Field Pinch," Phys. Rev. Lett. **85**, 3838 (2000).
[19] R. Lorenzini, E. Martines, P. Piovesan, D. Terranova, P. Zanca, M. Zuin, A. Alfier, D. Bonfiglio, F. Bonomo, A. Canton, S. Cappello, L. Carraro, R. Cavazzana, D. F. Escande, A. Fassina, P. Franz, M. Gobbin, P. Innocente, L. Marrelli, R. Pasqualotto, M. E. Puiatti, M. Spolaore, M. Valisa, N. Vianello, P. Martin, P. Martin, L. Apolloni, M. E. Puiatti, J. Adamek, M. Agostini, A. Alfier, S. V. Annibaldi, V. Antoni, F. Auriemma, O. Barana, M. Baruzzo, P. Bettini, T. Bolzonella, D. Bonfiglio, F. Bonomo, M. Brombin, J. Brotankova, A. Buffa, P. Buratti, A. Canton, S. Cappello, L. Carraro, R. Cavazzana, M. Cavinato, B. E. Chapman, G. Chitarin, S. Dal Bello, A. De Lorenzi, G. De Masi, D. F. Escande, A. Fassina, A. Ferro, P. Franz, E. Gaio, E. Gazza, L. Giudicotti, F. Gnesotto, M. Gobbin, L. Grando, L. Guazzotto, S. C. Guo, V. Igochine, P. Innocente, Y. Q. Liu, R. Lorenzini, A. Luchetta, G. Manduchi, G. Marchiori, D. Marcuzzi, L. Marrelli, S. Martini, E. Martines, K. McCollam, F. Milani, M. Moresco, L. Novello, S. Ortolani, R. Paccagnella, R. Pasqualotto, S. Peruzzo, R. Piovan, P. Piovesan, L. Piron, A. Pizzimenti, N. Pomaro, I. Predebon, J. A. Reusch, G. Rostagni, G. Rubinacci, J. S. Sarff, F. Sattin, P. Scarin, G. Serianni, P. Sonato, E. Spada, A. Soppelsa, S. Spagnolo, M. Spolaore, G. Spizzo, C. Taliercio, D. Terranova, V. Toigo, M. Valisa, N. Vianello, F. Villone, R. B. White, D. Yadikin, P. Zaccaria, A. Zamengo, P. Zanca, B. Zaniol, L. Zanotto, E. Zilli, H. Zohm, M. Zuin, R. mod team, and collaborators, "Self-organized helical equilibria as a new paradigm for ohmically heated fusion plasmas," Nature Physics **5**, 570–574 (2009).
[20] J. Sarff, A. Almagri, J. Anderson, M. Borchardt, W. Cappechi, D. Carmody, K. Caspary, B. Chapman, D. D. Hartog, J. Duff, S. Eilerman, A. Falkowski, C. Forest, M. Galante, J. Goetz, D. Holly, J. Koliner, S. Kumar, J. Lee, D. Liu, K. McCollam, M. McGarry, V. Mirnov, L. Morton, S. Munaretto, M. Nornberg, P. Nonn, S. Oliva, E. Parke, M. Pueschel, J. Reusch, J. Sauppe, A. Seltzman, C. Sovinec, D. Stone, D. Theucks, M. Thomas, J. Triana, P. Terry, J. Waksman, G. Whelan, D. Brower, W. Ding, L. Lin, D. Demers, P. Fimognari, J. Titus, F. Auriemma, S. Cappello, P. Franz, P. Innocente, R. Lorenzini, E. Martines, B. Momo, P. Piovesan, M. Puiatti, M. Spolaore, D. Terranova, P. Zanca, V. Davydenko, P. Deichuli, A. Ivanov, S. Polosatkin, N. Stupishin, D. Spong, D. Craig, H. Stephens, R. Harvey, M. Cianciosa, J. Hanson, B. Breizman, M. Li, and L. Zheng, "Overview of results from the MST reversed field pinch experiment," **55**, 104006 (2015).
[21] S. C. Jardin, N. Ferraro, and I. Krebs, "Self-organized stationary states of tokamaks," Phys. Rev. Lett. **115**, 215001 (2015).
[22] I. Krebs, S. C. Jardin, S. Günter, K. Lackner, M. Hoelzl, E. Strumberger, and N. Ferraro, "Magnetic flux pumping in 3d nonlinear magnetohydrodynamic simulations," Physics of Plasmas **24**, 102511 (2017).
[23] P. Piovesan, D. Bonfiglio, M. Cianciosa, T. Luce, N. Taylor, D. Terranova, F. Turco, R. Wilcox, A. Wingen, S. Cappello, C. Chrystal, D. Escande, C. Holcomb, L. Marrelli, C. Paz-Soldan, L. Piron, I. Predebon, and B. Zaniol, "Role of a continuous MHD dynamo in the formation of 3d equilibria in fusion plasmas," Nuclear Fusion **57**, 076014 (2017).
[24] F. Cattaneo and S. M. Tobias, "Dynamo properties of the turbulent velocity field of a saturated dynamo," Journal of Fluid Mechanics **621**, 205 (2009).
[25] A. Aydemir and D. Barnes, "Three-dimensional nonlinear incompressible mhd calculations," J. Comp. Phys. **53**, 100 (1983).
[26] D. Schnack, D. Barnes, Z. Mikic, D. Harned, E. Caramana, and R. Nebel, "Numerical simulation of reversed-field pinch dynam-

ics," Computer Physics Communications **43**, 17–28 (1986).

[27] J. Dahlburg, D. Montgomery, G. Doolen, and L. Turner, "Driven, steady-state rfp computations," Journal of plasma physics **40**, 39–68 (1988).

[28] S. Cappello and R. Paccagnella, "Nonlinear plasma evolution and sustainment in the reversed field pinch," Physics of Fluids B: Plasma Physics **4**, 611–618 (1992).

[29] P. Piovesan, D. Bonfiglio, M. Cianciosa, T. Luce, N. Taylor, D. Terranova, F. Turco, R. Wilcox, A. Wingen, S. Cappello, *et al.*, "Role of a continuous mhd dynamo in the formation of 3d equilibria in fusion plasmas," Nuclear Fusion **57**, 076014 (2017).

[30] M. Veranda, D. Bonfiglio, S. Cappello, D. F. Escande, F. Auriemma, D. Borgogno, L. Chacón, A. Fassina, P. Franz, M. Gobbin, *et al.*, "Magnetohydrodynamics modelling successfully predicts new helical states in reversed-field pinch fusion plasmas," Nuclear Fusion **57**, 116029 (2017).

[31] J. Morales, W. J. T. Bos, K. Schneider, and D. Montgomery, "The effect of toroidicity on reversed field pinch dynamics," Plasma Phys. Control. Fusion **56**, 095024 (2014).

[32] J. Morales, M. Leroy, W. J. T. Bos, and K. Schneider, "Simulation of confined magnetohydrodynamic flows with dirichlet boundary conditions using a pseudo-spectral method with volume penalization," J. Comp. Phys. **274**, 64–94 (2014).

[33] R. Chahine and W. J. T. Bos, "On the role and value of β in incompressible mhd simulations," Phys. Plasmas **25**, 042115 (2018).

[34] R. Grappin, U. Frisch, J. Leorat, and A. Pouquet., "Alfvenic fluctuations as asymptotic states of mhd turbulence." Astron. Astrophys. **105**, 6 (1982).

[35] M. Dobrowolny, A. Mangeney, and P. Veltri, "Fully developed anisotropic hydromagnetic turbulence in interplanetary space." Phys. Rev. Lett. **29**, 3261 (1980).

[36] S. Neffaa, W. J. T. Bos, and K. Schneider, "The decay of magnetohydrodynamic turbulence in a confined domain," Phys. Plasmas **15**, 092304 (2008).

[37] W. H. Matthaeus, A. Pouquet, P. D. Mininni, P. Dmitruk, and B. Breech, "Rapid alignment of velocity and magnetic field in magnetohydrodynamic turbulence," Phys. Rev. Lett. **100**, 085003 (2008).

[38] S. Servidio, W. H. Matthaeus, and P. Dmitruk, "Depression of nonlinearity in decaying isotropic mhd turbulence," Phys. Rev. Lett. **100**, 095005 (2008).

PLEASE CITE THIS ARTICLE AS DOI: 10.1063/5.0078860

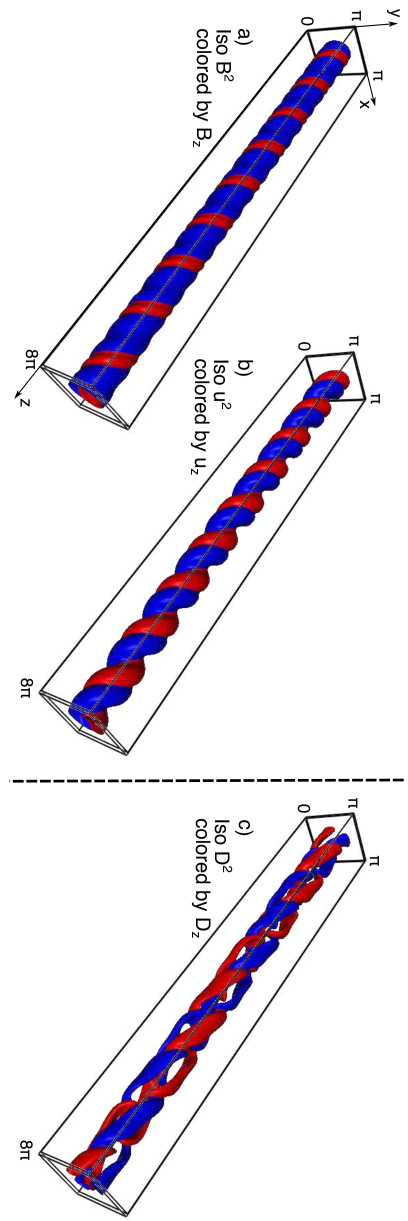

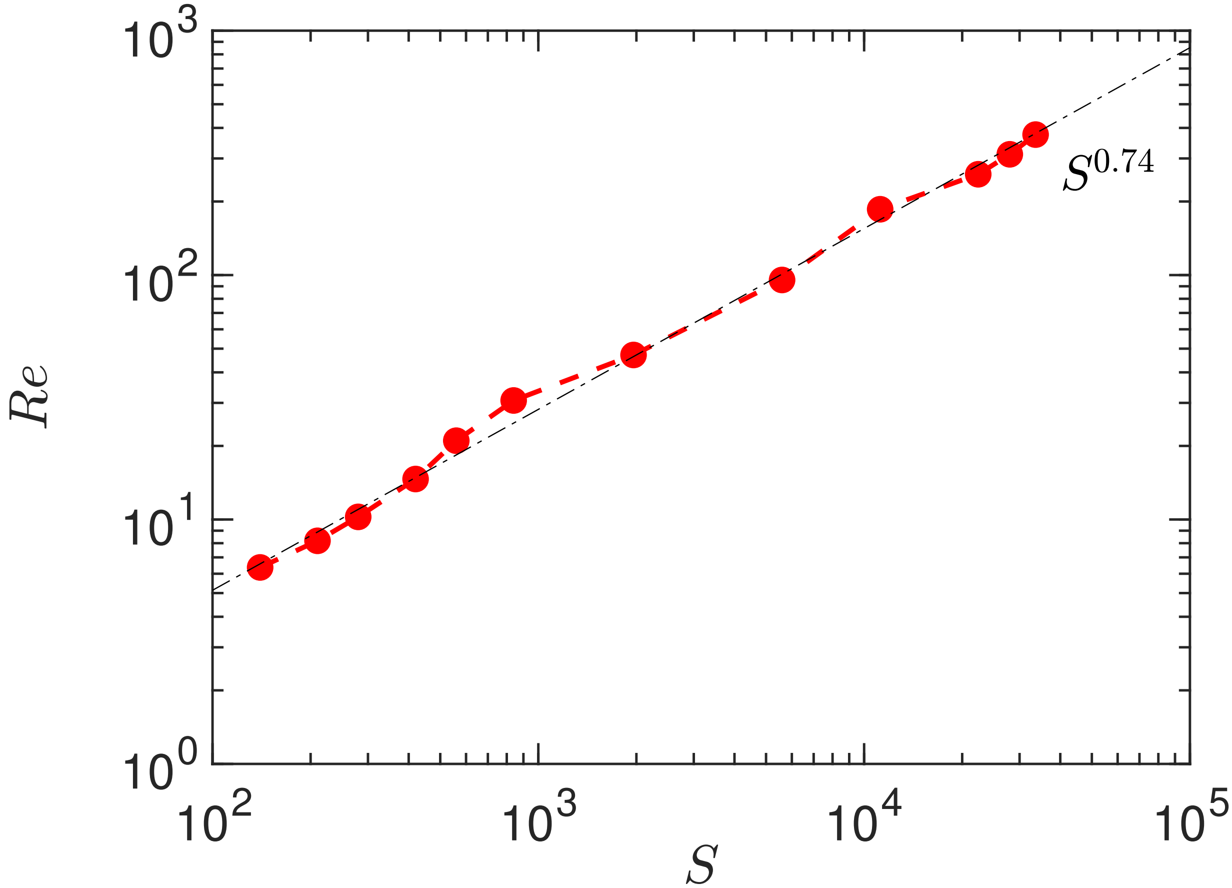
10^3
10^2
10^1
10^0
Re
$S^{0.74}$
10^2
10^3
10^4
10^5
S

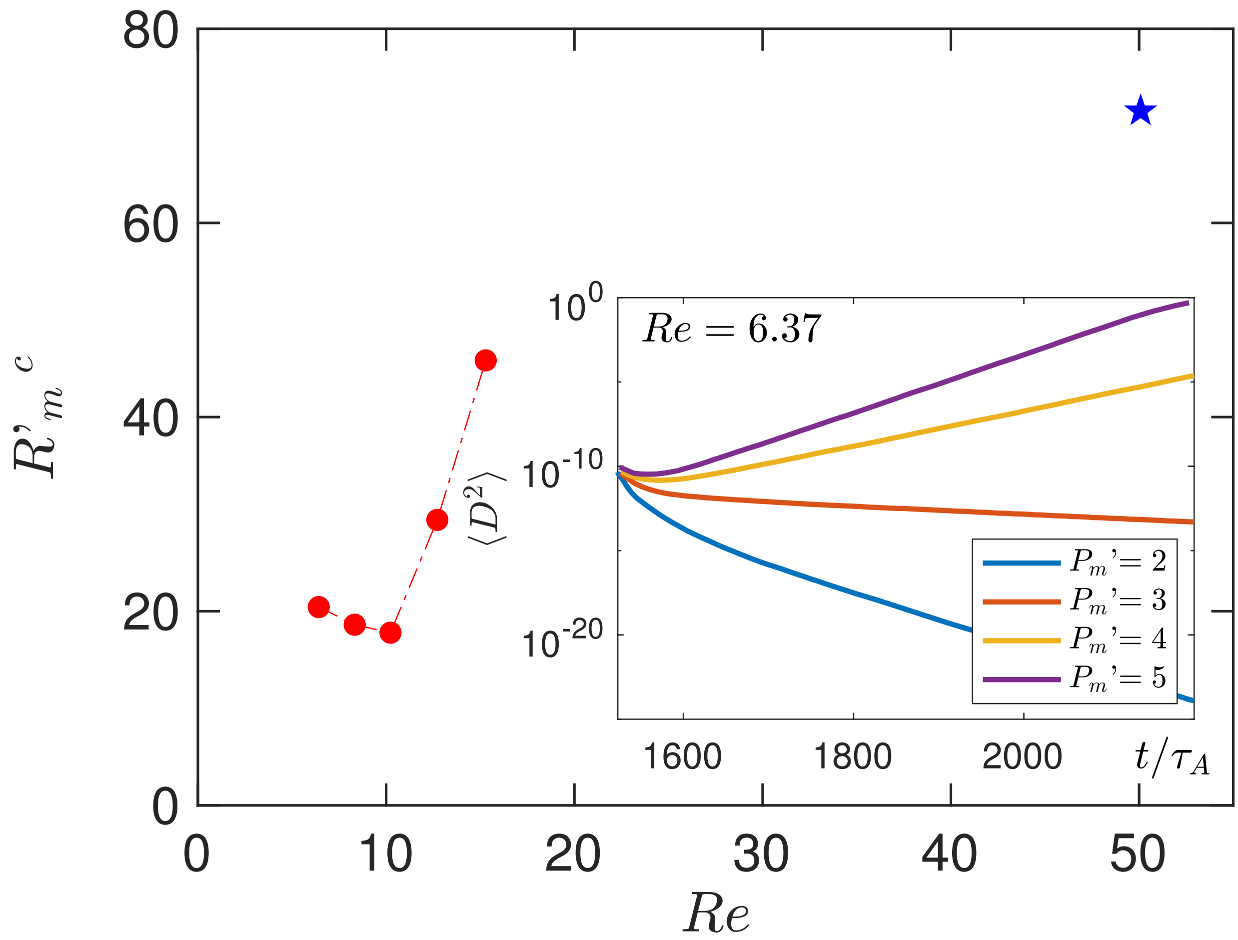
$R'_m{}^c$
Re
$Re = 6.37$
$\langle D^2 \rangle$
t/τ_A
$P_m' = 2$
$P_m' = 3$
$P_m' = 4$
$P_m' = 5$

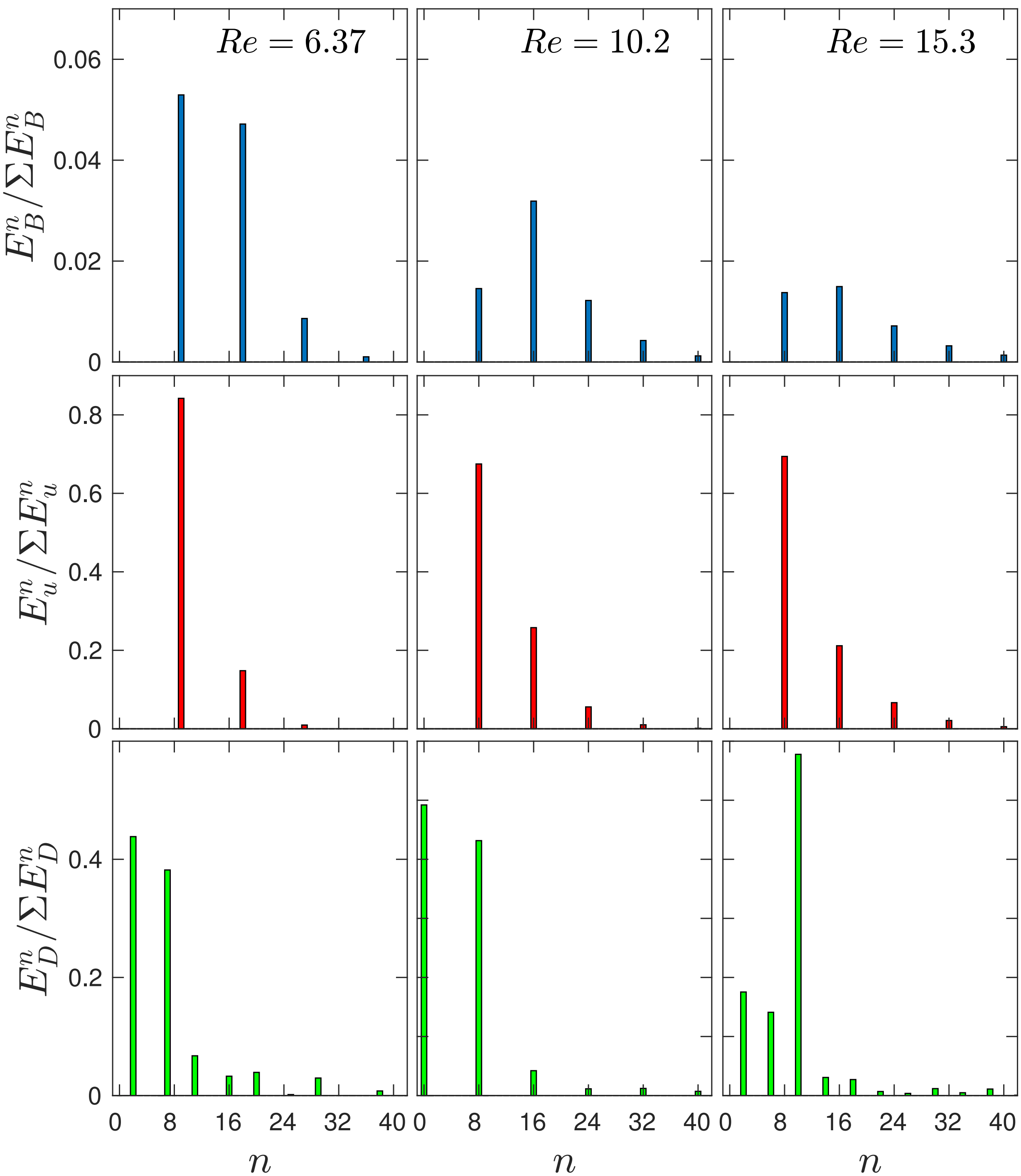
$Re = 6.37$
$Re = 10.2$
$Re = 15.3$
$E_B^n/\Sigma E_B^n$
$E_u^n/\Sigma E_u^n$
$E_D^n/\Sigma E_D^n$
0.06
0.04
0.02
0
0.8
0.6
0.4
0.2
0
0.4
0.2
0
0 8 16 24 32 40
n

AIP Publishing

Physics of Plasmas

ACCEPTED MANUSCRIPT

PLEASE CITE THIS ARTICLE AS DOI: 10.1063/5.0078860

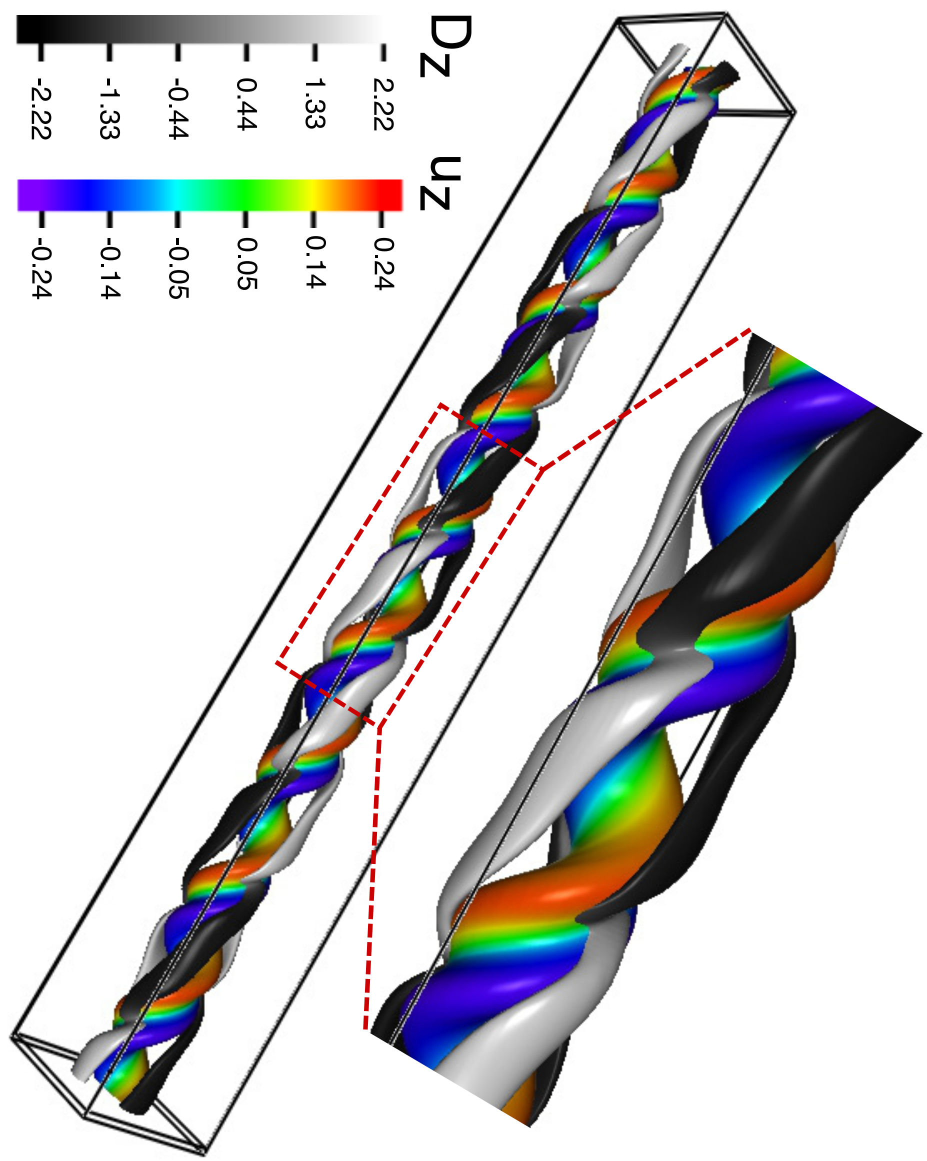

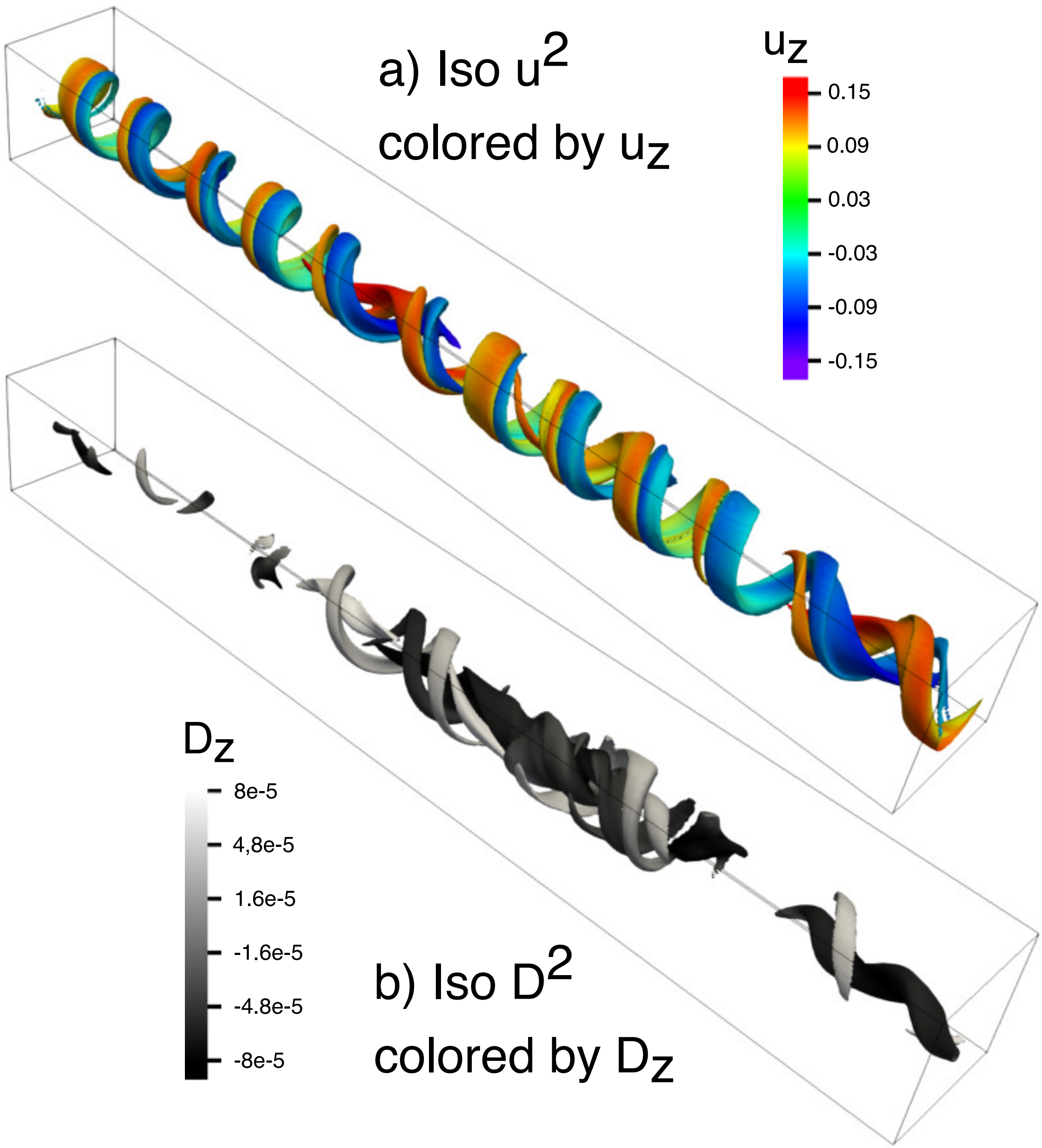
a) Iso u^2
colored by u_z
u_z
0.15
0.09
0.03
-0.03
-0.09
-0.15
D_z
8e-5
4,8e-5
1.6e-5
-1.6e-5
-4.8e-5
-8e-5
b) Iso D^2
colored by D_z

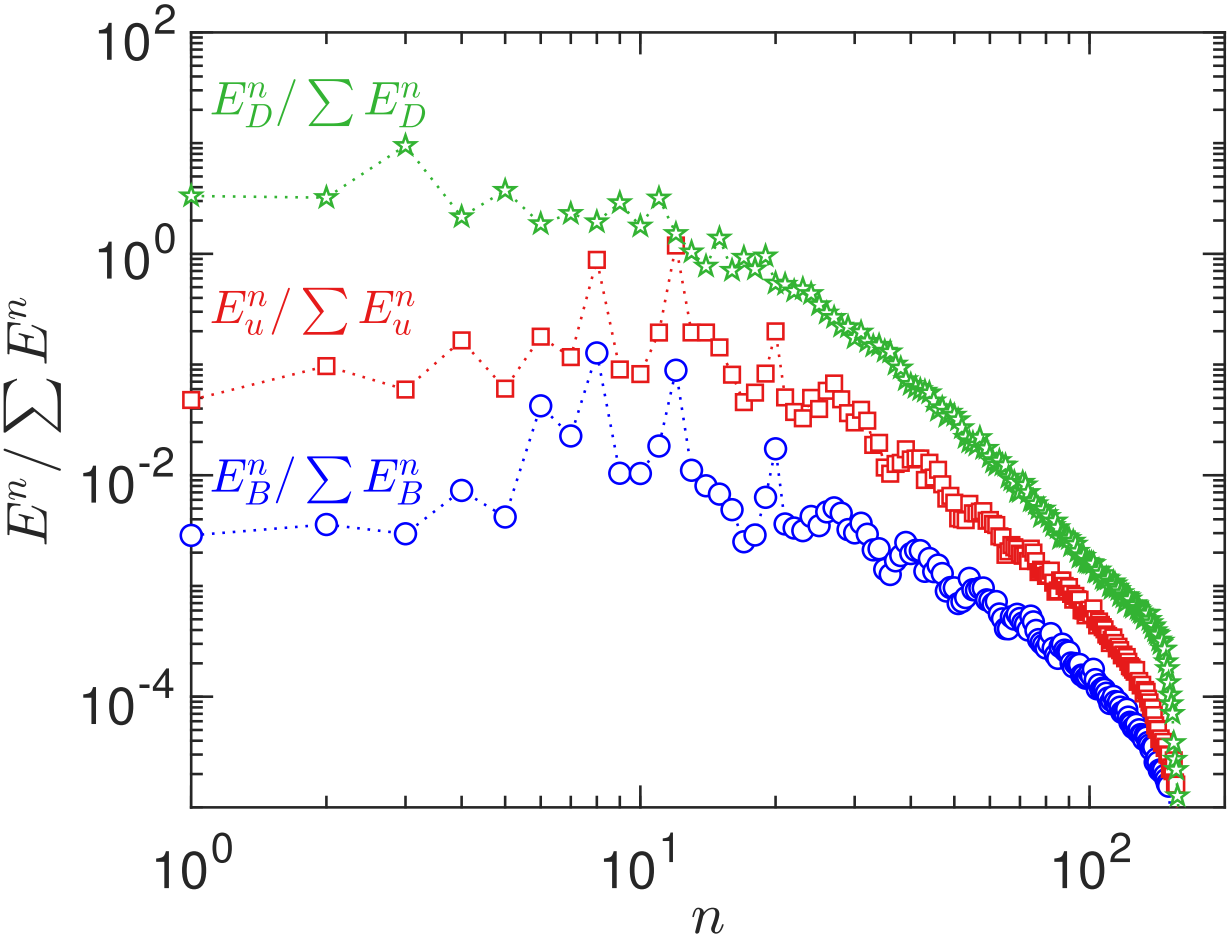
$E_D^n / \sum E_D^n$
$E_u^n / \sum E_u^n$
$E_B^n / \sum E_B^n$
$E^n / \sum E^n$
n
10^2
10^0
10^{-2}
10^{-4}
10^0
10^1
10^2

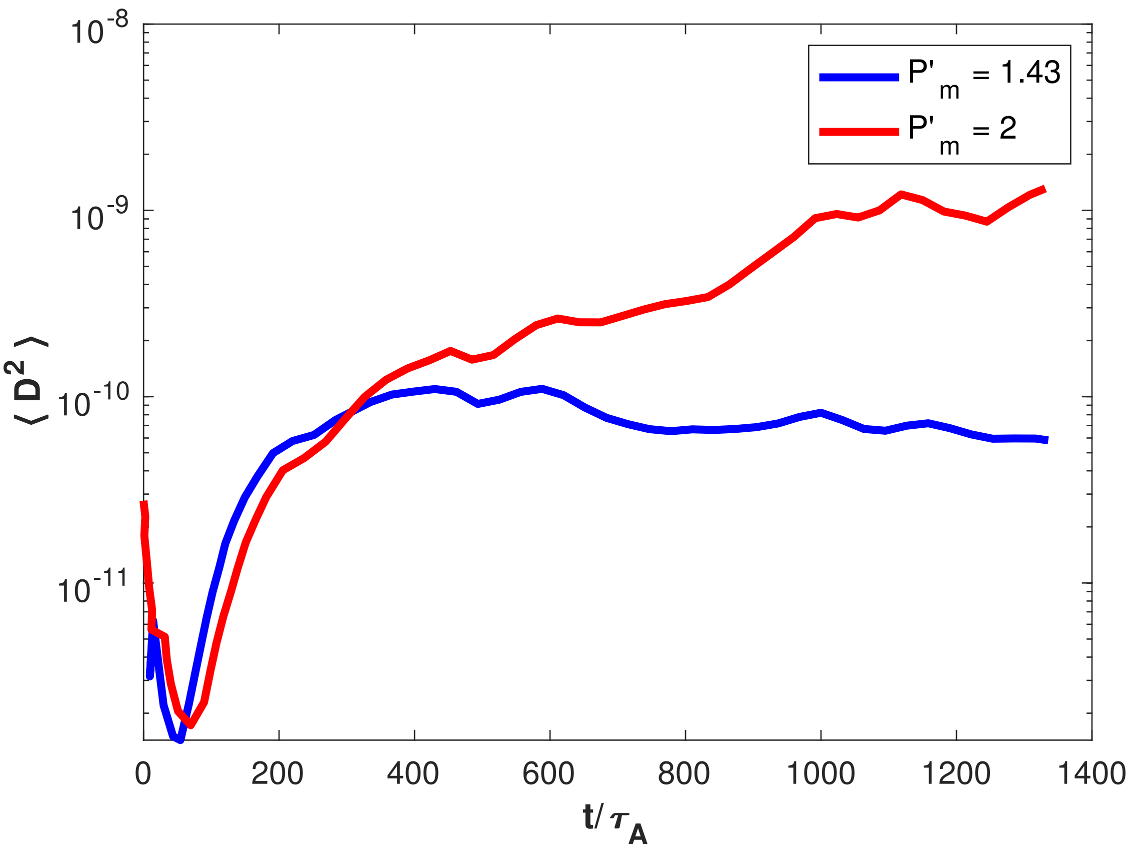
$P'_m = 1.43$
$P'_m = 2$
10^{-8}
10^{-9}
10^{-10}
10^{-11}
$\langle D^2 \rangle$
0
200
400
600
800
1000
1200
1400
t/τ_A

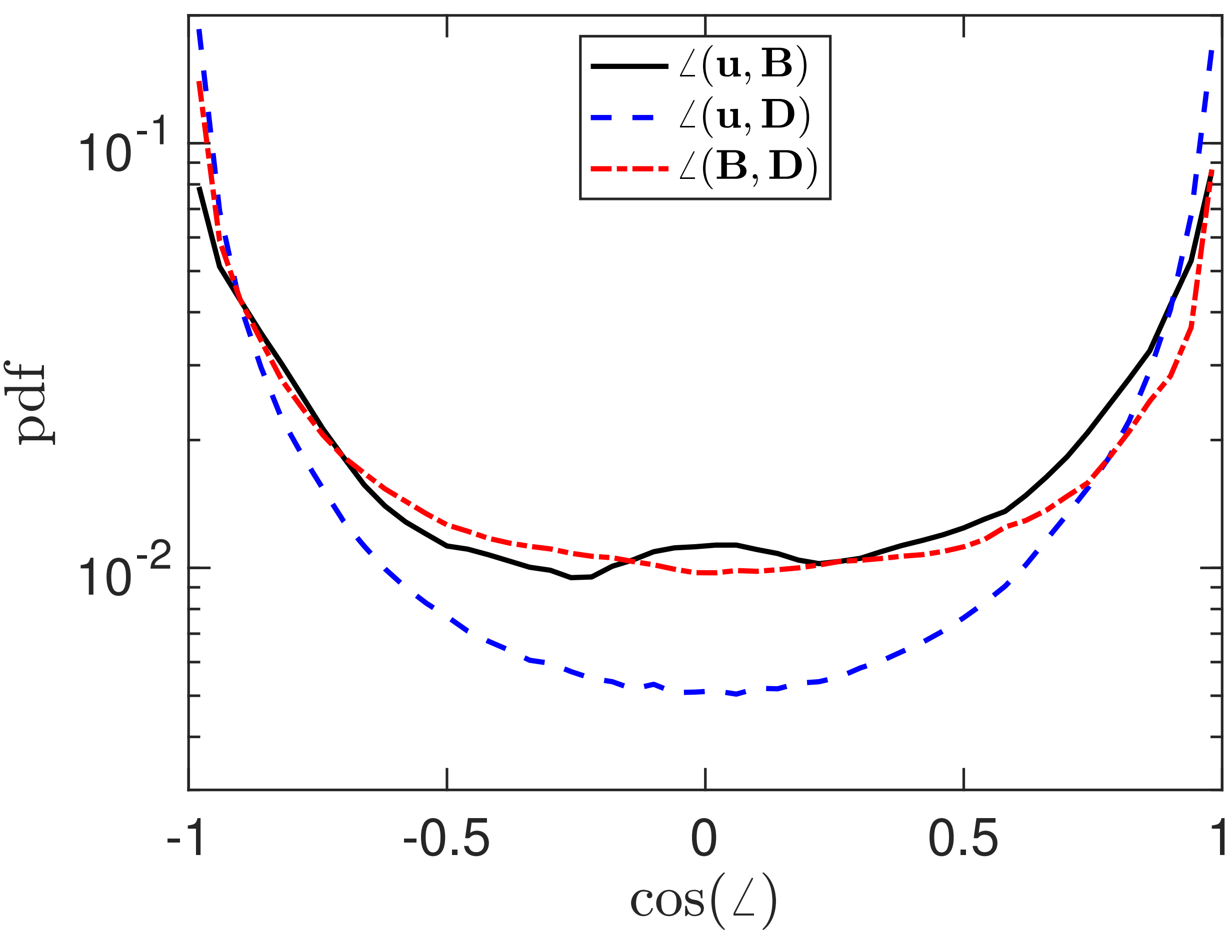
$\angle(\mathbf{u},\mathbf{B})$
$\angle(\mathbf{u},\mathbf{D})$
$\angle(\mathbf{B},\mathbf{D})$
10^{-1}
10^{-2}
pdf
-1
-0.5
0
0.5
1
$\cos(\angle)$